Generation of Graphite Particles by Rotational/Spinning Abrasion and Their Characterization

A Thesis Presented to

The Faculty of the Graduate School

At the University of Missouri

In Partial Fulfillment

Of the Requirements for the Degree

Master of Science

By

RAYMOND STEVEN TROY

Dr. Robert Tompson, Thesis Supervisor

MAY 2011

The undersigned, appointed by the dean of the Graduate School,

have examined the thesis entitled

Generation of Graphite Particles by Rotational/Spinning Abrasion and Their Characterization

Presented by Raymond Steven Troy

A candidate for the degree of

Master of Science

And hereby certify that, in their opinion, it is worthy of acceptance.

_____

Professor Sudarshan Loyalka

_____

Professor Robert Tompson

_____

Professor Tushar Ghosh

_____

Professor Mark Prelas

_____

Professor Dabir Viswanath

ACKNOWLEDGEMENTS

TABLE OF CONTENTS

Chapter

TABLE OF FIGURES

Figure   Page

Table of Tables

Table   Page

ABSTRACT

Graphite particle generation by inter-pebble abrasion and by abrasion of pebbles with the containment vessel during operation of a Pebble Bed Reactor (PBR) is an issue of interest in the safety analysis of this class of Very High Temperature Reactor (VHTR). To understand particle generation, we have constructed an apparatus to generate graphite particles from preformed graphite hemispheres under rotational/spinning abrasive loading. We have initially used commercial grade graphites in our experiments and have generated size distributions for the abraded particles, determined particle shapes, and have measured the particle surface areas, pore volumes, and pore volume distributions of particles produced during abrasion of graphite surfaces under different conditions. The size distributions were studied using an Aerodynamic Particle Sizer™ (APS™) and a Scanning Mobility Particle Sizer™ (SMPS™). Most of the particles observed were in the range from 18.1 to 600 nm in diameter. The SEM micrographs showed that the particles tend to be irregular in shape and porous in nature. We have also conducted BET surface area and pore volume measurements that have verified the highly porous nature of the particles. The calculated surface area and porosity for our initial measurements of the particles from this particular grade of commercial graphite were found to be 626 m^2 gm^{-1} and 68%, respectively.

I. INTRODUCTION

The Pebble Bed Reactor (PBR) is one configuration of a Very High Temperature Reactor (VHTR) in which graphite dust particles can be produced due to inter-pebble abrasion and abrasion of the pebbles with the containment vessel during normal operation. Graphite dust particles can also be produced during the online refueling of the pebbles. Understandings of the amounts of such particulate material (dust) produced in a PBR and the shape and size of the constituent particles are important to the safe operation of the plant, its maintenance, and also for the licensing of these reactors. The PBR uses tri-isotropic or tri-structural-isotropic (TRISO) fuel wherein small kernels of fuel (UO_2 or UCO) are coated with multiple layers of materials of varying thickness and morphology. Typically these layers would include an innermost layer of amorphous carbon, a second layer of dense pyrolytic carbon, a third layer of ceramic SiC and an outer layer of additional dense pyrolytic carbon.[1] A number of variants of this type of fuel have been studied but the typical size of a coated fuel particle is generally about 0.5 mm in diameter. In the pebble bed configuration, a number of these coated fuel particles (typically about 15,000) are then embedded in a matrix of graphite formed into a spherical pebble about the size of a tennis ball. In a typical pebble bed reactor, the core then consists of about 360,000-380,000 of these pebbles randomly distributed in a pebble bed filling the inside of a containment vessel where refueling is a simple function of removing used pebbles from below while fresh pebbles are dropped in from above. Cooling is effected by the passage of an inert coolant gas (typically He) through the bed. Although TRISO fuel is very robust, fission products can diffuse through the various layers of the TRISO fuel particles and the surrounding graphite pebble and end up in the

graphite particles that are produced by abrasion of the pebbles as they move through the core. This graphite particle dust interacts (absorption, adsorption, reaction) with fission products (FP, gases, vapors and solids) and can act to either facilitate or hinder their transport. The dust can remain in suspension, settle at the bottom of the reactor vessel, or deposit throughout the coolant loop. In the case of an accident, the dust particles would then be subject to release to the containment (through re-suspension) and possibly to the environment. In order to determine the role of the dust particles in fission product transport, information about the dust particles, such as their shape and size distributions, needs to be known. Information regarding the production of these dust particles may also be needed for licensing, for accident prevention and mitigation, for determinations of deposition and plateout in the reactor systems, and for maintenance purposes.

The first PBR was constructed in Germany (Arbeitsgemeinschaft Versuchsreaktor Julich (AVR) GmBH) and was operated from 1967 to 1988. When it was decommissioned in 1988, roughly 60 kg of graphite particle dust was found distributed throughout the reactor.[2] This amount was substantially higher than what had been expected.

Air ingress to a PBR core pipe breakage or during an accident can be a significant problem since graphite has a tendency to burn in air as was observed during the Windscale accident and this tendency is exacerbated for graphite dust particles due to their relatively high surface to volume ratios. Bach *et al.*[3] noted that graphite dust particles have a much higher probability of combustion than a solid block of graphite due to this increased surface area and have greater ease of mobility. Depending upon the number and size of the dust particles, coolant pumps can also potentially get clogged

causing a major problem. The dust particles can settle or plateout in the heat exchanger due to diffusion, thermophoresis, and other aerosol transport mechanisms thus fouling the heat exchanger surfaces and resulting in heat transfer complications in the PBR system. In order to properly model all of these behaviors, knowledge of the various properties of the graphite dust particles is required. Ball *et al.* [4] and Bisplinghof *et al.*[5] have indicated that the safety of the workers performing maintenance on the reactor can also be tied to the properties of the graphite dust particles.

We review below some of the previous work on graphite particle generation and characterization. Saishu and Inoue[6] generated graphite dust particles by cutting graphite blocks with a band saw and by rubbing blocks together when removing them from a core. Their research focused on ways to possibly dispose of irradiated or contaminated graphite from High Temperature Reactors (HTRs). They studied the particles generated from sawing including both the minute particle dust floating in the atmosphere as well as the dust collected on the floor. They observed a particle distribution from 0.06 µm to 250 µm in diameter with a large percentage of their findings in the 4 to 45 µm range. Luo Xiaowei *et al.*[7] studied the effects of temperature on the coefficient of friction on IG-11 reactor grade graphite. Their experiments were designed to test graphite-graphite and graphite-stainless steel wear at different temperatures. The graphite dust particles generated were collected and the worn surfaces and debris were observed with a Scanning Electronic Microscope (SEM) where the distribution of the wear debris particles was analyzed by EDX particle analysis software. It was found that there were different wear mechanisms at different temperatures. The main wear mechanism at room temperature was abrasive wear, while at 473 K it was fatigue wear, and at 673 K it was

adhesive wear. This difference was mainly due to changes in the stress distribution in the contact area. A study by Sheng et $al.$[8] produced graphite particles with line contact (30 mm) and surface abrasion (804 mm^2). Most of the particles generated were small and approximately spherical but there were a few large particles with flake shapes. The average wear rate under surface contact was 2.27×10^{-7} gm min^{-1} for the first 4000 min under a load of 31 N and a sliding velocity of 0.54 m sec^{-1}. After 4000 sec, the wear rate changed for different specimens, thus showing that time has a large effect on the wear rate. Under line contact, the wear rate was 1.02×10^{-6} gm min^{-1} for a load of 31 N and 1.99×10^{-6} gm min^{-1} for a load of 62 N while both had a sliding velocity of 0.78 m sec^{-1}. For the surface contact particles the area of the particles was measured using EDX software and SEM images. Nearly 60% of the particles were less than 5 μm^2 in cross sectional area. Only 3-5% of the particles had areas greater than 30 μm^2. The largest observed particle was 1036.9 μm^2 and the average area was 7.26 μm^2. Although 60% of the particles were less than 5 μm^2, the average area was not in this range due to some extremely large particles having areas greater than 30 μm^2. Particles from the line contact experiment had roughly the same distribution. The average particle area was 10.76 μm^2 and more than 40% of the particles were in the range less than 5 μm^2. The higher average area of particles under line contact demonstrates the severe wear that can occur under line contact.

There has been much research into the coefficient of friction under different conditions but there has been no connection made between the coefficient of friction and the dust particle production.[9-14] In other work, Forester et $al.$[15] dropped one pebble onto another pebble which gave insights into the products of binary collisions between

spheres. Holmes *et al.*[16] studied the microscopic and macroscopic surface features of the particles generated by rocking a single graphite brick which gave insights into the stress distributions for flat surfaces mating to hemispherical surfaces with relative motion.

II. EXPERIMENTS

In the present work, we designed and built an apparatus that allowed generation of graphite dust particles by simulating the rotational wear/abrasion that is likely to occur in a pebble bed reactor. While this is not the only type of abrasion possible and does not exactly mimic the forces exerted on the pebbles during routine operation, it provides insights into the generation mechanisms of graphite dust particles and the effects of various parameters that may influence the particle generation process and the size distributions of the particles produced. The system was designed to study the effect of various parameters such as loading, speed of rotation, atmosphere, shape of interacting surfaces, and types of graphite. In this work, we changed the loading and rotational speeds while keeping the shape of the interface, the atmosphere, and the type of graphite constant. A Scanning Mobility Particle Sizer™ (SMPS) was used for size distributions from 18.1 nm to 514 nm and an Aerodynamic Particle Sizer™ (APS) was used for measuring particles from 530 nm to 20,000 nm. Due to the way the SMPS™ and APS™ instruments are designed, the SMPS™ measures the electrical mobility diameter of particles and the APS™ measures aerodynamic particle diameter. Electrical mobility is the velocity per unit electrical field strength, or intensity E, of a charged particle in a medium. This is the same as the charge on the particle, q, times the mechanical mobility, B. Aerodynamic diameter is the diameter of an 'equivalent' unit-density

spherical particle that has the same settling velocity as the actual particle.[17] The TSI Inc. data merge software was used to combine the two sets of data into one set along a common axis as well as to perform a fit to the raw experimental data so that it can be used in modeling. The equation used in relating these two values so they can be plotted on a common axis is given here:

$$d_a = d_m \left[\frac{C_C(d_m)}{C_C(d_a)} \right]^{\frac{1}{2}} \left(\frac{\rho_p}{\chi \rho_0} \right)^{\frac{1}{2}}$$

(1)

where d_a is the aerodynamic particle diameter, d_m is the electrical mobility particle diameter, ρ_p is the particle density, ρ_0 is the default reference density taken to be 1 gm cm^{-3} in this instance, χ is the dynamic shape factor, and $C_C(d_p)$ is the Cunningham slip correction factor which is expressed as:

$$C_C(d_p) = 1 + \frac{2\lambda}{d_p} \left(1.142 + 0.558 \exp \left(\frac{-0.999 d_p}{2\lambda} \right) \right)$$

(2)

where λ is the gas molecular mean free path and d_p is the particle diameter.[18] For our work, we used a mean free path of 6.65×10^{-8} m. There are many different forms of Cunningham slip corrections in the literature[19], but they all lead to similar values. All of our size distributions are displayed in terms of the aerodynamic particle diameter. The shapes of the abraded particles were determined by Scanning Electron Microscope (SEM), and the BET (Brunauer-Emmett-Teller) surface areas of the particles produced were determined using a surface area analyzer (Model Quantachrome-Autosorb 1). The adsorption isotherm obtained from the surface area analyzer was further used to calculate total pore volume and the pore size distribution.

II.A. Materials.

The graphite hemispheres used in this study were obtained from Graphtek LLC. Very fine grain, isomolded, graphite powder was isostatically pressed into hemispheres with a plug hole for mounting the sample to the sample holder. The diameters of the molded hemispheres were 5 cm. Various properties of the graphite studied are provided in Table I. A threaded insert was screwed into each plug hole so that the graphite hemispheres could be mounted either onto the sample holder or in the chuck of the mill that produced the loaded rotation. The inserts were machined 0.001 inch larger than the internal diameter of the plug holes to provide an interference fit that prevented the hemispherical samples from misaligning as well as providing enough friction to prevent the machined insert from rotating inside the sample. A photograph of one sample with its threaded insert is shown in Fig. 1.

Fig. 1. Graphite hemispherical sample mounted on a shaft.

TABLE I

Properties of the graphite used (hemispherical sample)

Manufacturer	Graphtek, LLC
Method of manufacture	Isostatically pressed
Description /Property	Isomolded, very fine grain, high strength, low ash graphite with superior oxidation resistance.
Density	1750 kg m^{-3}
Particle size	38.1 μm
Flexural strength	59.1 MPa
Compressive strength	98.5 MPa
Resistivity	2.17×10^{-6} Ohm m
CTE	3.8×10^{-6} K^{-1}
Porosity	13.2 %
Thermal conductivity	9 W m^{-1} K^{-1}
Ash content	0.01 %

II.B. Test Bed.

The design of the experimental test bed is shown schematically in Fig. 2. Two hemispheres were used in the experimental runs. One of the hemispheres (the lower one) was stationary and was in contact at a single point with the other hemisphere which was rotated under load by a milling machine producing a pure rotational abrasion at the contact point. The test bed was outfitted with a constant tensioning device so that, as the hemispheres wore, the load would remain constant. The sample holder and scale, which measured the loading, sat on the deck of the milling machine.
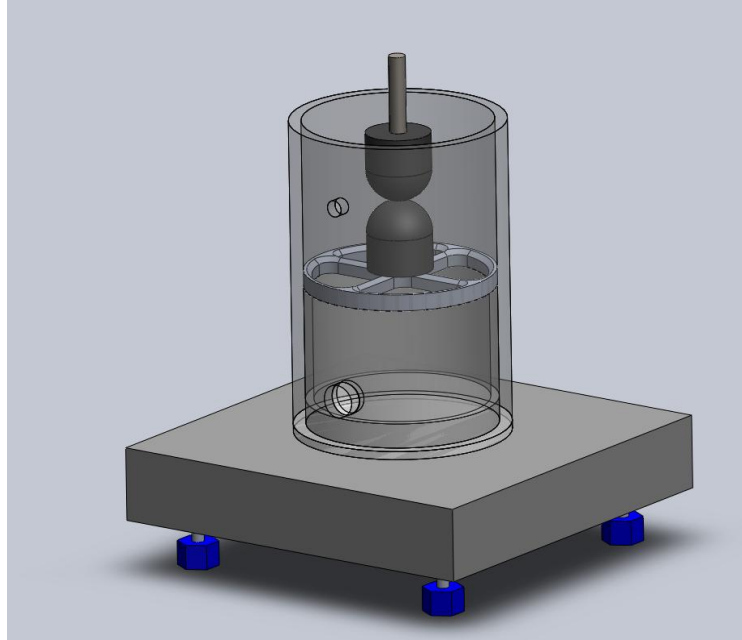
Fig. 2. Experimental setup showing loading and rotation.

The test bed was constructed using a clear acrylic pipe to observe the particle generation during experimentation. It is machined on the top and bottom to ensure stability as well as the alignment of the two graphite spheres. It is 15.24 cm in diameter and uses a smaller diameter clear acrylic pipe at the base to support the sample holder. This provides the flexibility of the test bed allowing for different collection methods as well as easy adjustment of the sample holder height. The flat top and flat base of the test bed are also made of clear acrylic. All surfaces were machined to assure stability and alignment of the samples. The top plate has a hole reamed to high tolerance to accept an interference fit with a bronze bushing which adds stability to the rotating shaft, helps to align the test samples, eliminates leakage of the entrainment gas flow and prevents frictional heating of the acrylic chamber during rotation of the shaft. This increased stability further prevented any sliding abrasion in conjunction with the rotational abrasion

due to misalignment. The sample holder was made out of aluminum and is designed to allow the abrasion generated particles to flow freely into the particle size distribution measurement system. The leading edges of the sample holder are knife edged to help prevent particles from settling on the sample holder. A photograph of the experimental system is shown in Fig. 3.
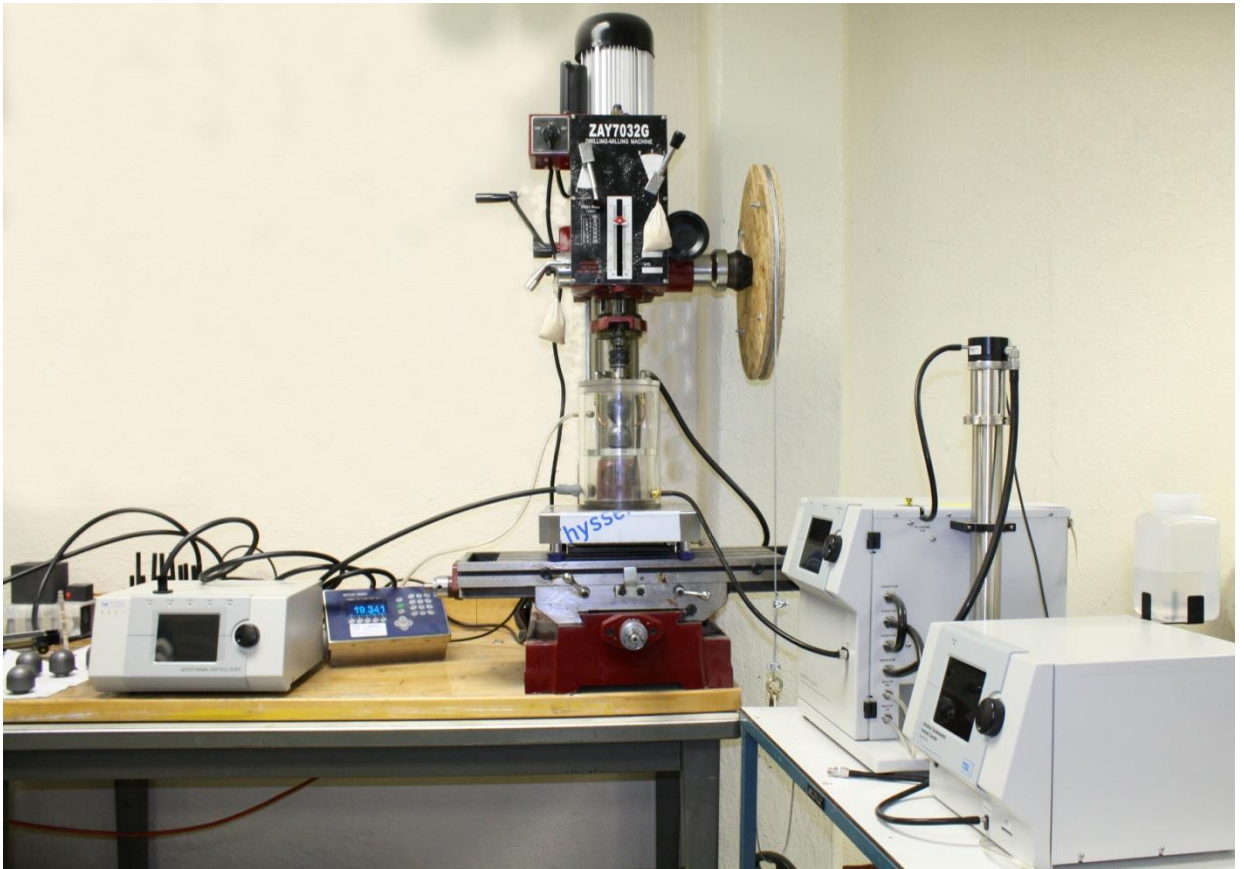

Fig. 3. Experimental test-bed.

The rotational speeds of the shaft were preset according to the milling machine manufacturer's specifications. The milling machine was a Central Machinery Geared Head Drill/Mill Machine model number 42827. The loading between the two hemispheres is measured by a Mettler Toledo balance; model number PBA 430, with an

IND 56 readout having an accuracy of ±0.001 kg with a maximum capacity of 60 kg.

II.C. Test Procedure.

Before each test the whole apparatus was dismantled and cleaned using propanol to ensure no residue or particles from any previous test were still in the apparatus. The device was reassembled and two new hemispherical graphite samples were loaded. Five blank runs on both the SMPS™ and APS™ were performed to ensure clean air inside the chamber. Then, a number of background runs were conducted with samples in place under load but without the rotation of the shaft. Rotation was initiated, and data collection started. At the end of the test, dust particles that did not get drawn into the SMPS™ and APS™, but which settled on the bottom of the cylinder, were collected and viewed under a scanning electron microscope (SEM) to determine the shapes of the particles. These settled samples were further analyzed for their surface area, pore volume, and pore size distribution.

II.D. Data Analysis.

The particle size distribution was measured by a TSI Scanning Mobility Particle Sizer™ (SMPS™) in conjunction with a TSI Aerodynamic Particle Sizer™ (APS™). Two ports were machined into the cylinder to allow particles to be drawn into the particle sizers. As the particles were produced, they were entrained in air and were carried to the TSI Scanning Mobility Particle Sizer™ (SMPS™) as well as to the TSI Aerodynamic Particle Sizer™ (APS™) by the internal pumping systems in the equipment. The SMPS system draws 2.4 L min^{-1} of particle laden gas into the machine and the APS™ draws 5

L min^{-1}. The SMPS™ is capable of measuring electrical mobility diameters in the range 2.5 nm to 1000 nm while the APS™ has a capability of measuring aerodynamic diameters from 500 nm up to 20,000 nm. In our experiment, the SMPS™ measured particle diameters from 18.1 nm to 514 nm, while the APS™ measured particle diameters 530 nm to 20,000 nm. The SMPS™ consists of an Electrostatic Classifier (EC), TSI model number 3080, and a Condensation Particle Counter (CPC), TSI model number 3776, housed in the same piece of equipment. The EC and CPC are used in conjunction to create particle size distributions. TSI model 3321 Aerodynamic Particle Sizer™ (APS™) provides high-resolution, real-time aerodynamic diameter measurements by measuring light-scattering intensity.   This device complies with standard ISO 15900:2009.

The shapes of the graphite particles were determined from SEM micrographs. A FEI Quanta 600 FEG Extended Vacuum Scanning Electron Microscope (ESEM) was used to take images under a high vacuum ($<6\times10^{-4}$ Pa). The Brunauer, Emmett and Teller (BET) surface area, pore volume, and pore size distribution of the graphite dust particles generated in this work were determined using a Quantachrome Autosorb-1 surface area analyzer at 77 K (liquid nitrogen temperature).

II.E. Experimental Matrix.

The experiments were conducted at the prevailing room temperature and humidity using filtered room air. The filter used was a HEPA filter (TSI, model 1602051) which captures 99.97% of particles greater than 0.3 µm. Since both temperature and humidity can potentially have significant effects on the wear of graphite and, hence, on abrasive

particle generation,[15] prior to each run, the room humidity and temperature were recorded. No attempt was made in these initial experiments, however, to conduct the experiments under specific temperature and humidity controlled conditions.

The loadings and rotational speeds were the only variables considered in the present experimental runs. The test matrix is given below.

TABLE II

Experimental Test Matrix

Test No.	Loading (kg)	Rotational speed (rpm)	Time (min)
1	60	1500	13
2	31	1500	13
3	10	1500	27
4	22	310	25

The ranges of the loadings were chosen based on the loading that is expected in a PBR. The maximum loading will most likely occur when there is a vertical column of pebbles directly above the lowest pebble before it leaves the reactor. Assuming the common radius of the spherical pebbles in a PBR is 60 mm, that the density of the pyrolytic graphite composing the bulk of the pebbles is 2.18 gm cm^{-3}, and that each pebble contains, additionally, about 7 gm of fissile material, we calculated that the maximum load exerted on the bottom pebble of a pebble stack, which is the height of the core, would be around 50 kg. While approximate, this value is likely representative of the load that might be realized on a single pebble for both the Chinese HTR-PM 250 MWth and the PBMR-400 as they both have essentially the same designed core heights. The

Chinese HTR-PM 250 MWth reactor is cylindrical, about 11 m tall, and with a radius of 3 m. The PBMR-400 is designed to be annular, 11 m tall, and have an outer radius of 3.7 m and an inner radius of 2 m.[20,21] These are approximate calculations of the anticipated maximal loading that were used to select a balance for the load measuring which would have sufficient capacity and maximal accuracy. Based on these assumptions, we expect that the maximum loading on any given pebble will not typically exceed 60 kg during normal operating conditions. Further, we note that the loading value of 60 kg calculated here is probably conservative as we have ignored the frictional load bearing capability of the structure, as well as, the buoyancy of the pebbles in the coolant and the net upwards force on the pebbles that might be realized from the flow of the coolant. Further, we have not considered the pebble packing factor in the calculation. However, Ougouag and Terry[22] reported a packing factor between 60% to 62%.[22] This suggests that a purely vertical pebble column is not likely to occur.

III. RESULTS AND DISCUSSION

Graphite dust particles generated in this work were characterized by various methods to gain a better understanding of the morphology and characteristics of these particles. Two systems, APS™ and SMPS™, were used to determine the particle size distribution over a combined range of 18.1 to 20,000 nm. Some particles settled at the bottom of the chamber, which were analyzed for their shape and size, surface area, and pore size and pore volume distribution. Although we measured particle size up to 20,000 nm (20µm), almost no particles were observed in the range above 800 nm. Thus, we have displayed

distributions only up to the 800 nm to provide a better resolution to the shape and size of the distribution. These results are discussed further in the following sections.

III. A. Size distributions from SMPS™ and APS™.

The size distributions of graphite dust particles under various loadings as measured by the APS™ and SMPS™ systems are discussed below. These distributions were for the particles that remained entrained in air, and were carried away to APS™ and SMPS™ systems using their own sampling pump-systems. In all these experiments, the rotational speed of the shaft was kept constant at 1500 rpm (revolutions per minute) except during one run where it was 310 rpm. Figure 4 shows the particle size distribution under a 10 kg load at a rotational speed of 1500 rpm.
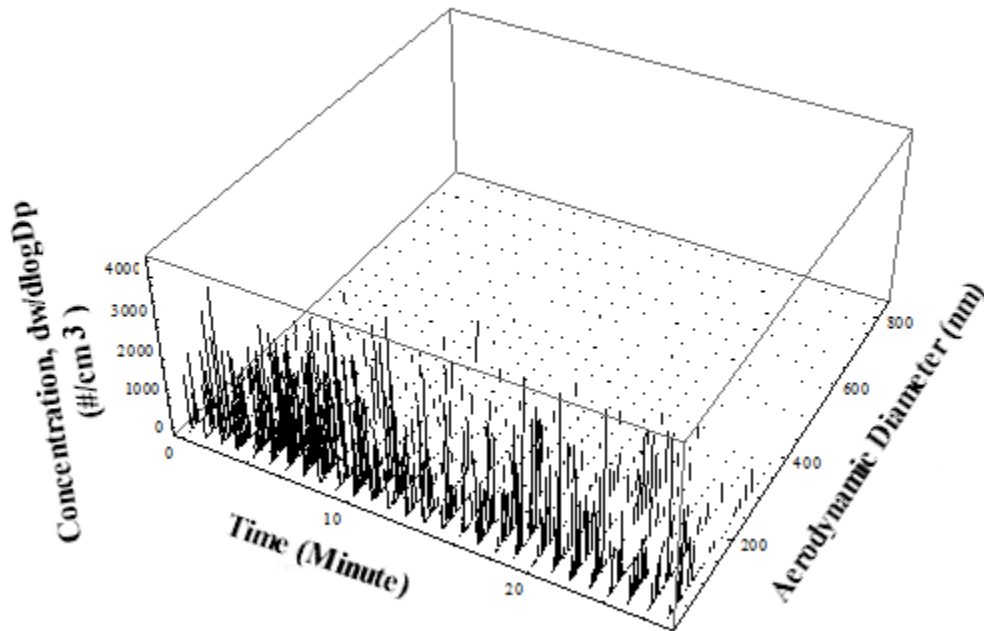

Fig. 4. Particle size distribution for 10 kg and 1500 rpm. The room temperature and average relative humidity were 303 K and 54%, respectively. This graph has been corrected for background.

The particle generation rate and the size distribution remained more or less constant for the entire test. However, it appears that the particle concentrations at this loading and rotational speed are very close to the background level. All the particles were small in size, and there were hardly any particles observed over 400 nm. Additional analysis of the data can be seen in Table III.

TABLE III

Mean, Standard Deviation, and Median of Particle Size Distribution (diameter in nm) at 10 kg Loading.

10 kg			
Time (min)	Mean	Standard Deviation	Median
0	93	86	83
1	109	109	54
2	83	72	62
3	92	80	54
4	86	73	50
5	89	68	62
6	75	59	50
7	69	45	58
8	99	76	67
9	87	94	67
10	83	88	46
11	86	66	67
12	83	67	50
13	88	75	62
14	82	75	40
15	93	81	50
16	120	95	103
17	82	65	54
18	100	53	83

19	100	80	72
20	83	49	67
21	100	91	67
22	76	64	62
23	143	93	159
24	98	82	54
25	70	58	58
26	102	63	77
27	120	96	83

Time does not seem to play a major role in the mean, standard deviation, and median of the distribution at this loading.

When the load was increased to 31 kg as shown in Fig. 5, and then to 56 kg as shown in Fig. 6, no significant particle generation was noted during an initial time period. Under a 31 kg load particle generation started only after about 6 minutes and the particles were less than 1000 nm in diameter with a significant number of particles in the 18.1 to 50 nm range. These nanoparticles continued to be produced during the entire length of the experimental run. A distinct pattern for the size distribution was not observed. As one can see at around 9 minutes into the test a large number of particles were released in a short period of time. This phenomenon was noted in the IAEA technical document of the AVR reactor.[2] It was also noted that the size distribution and the changes in the number of particles with time is an indication that the existing wear has a strong effect on particle generation rate as well as size.
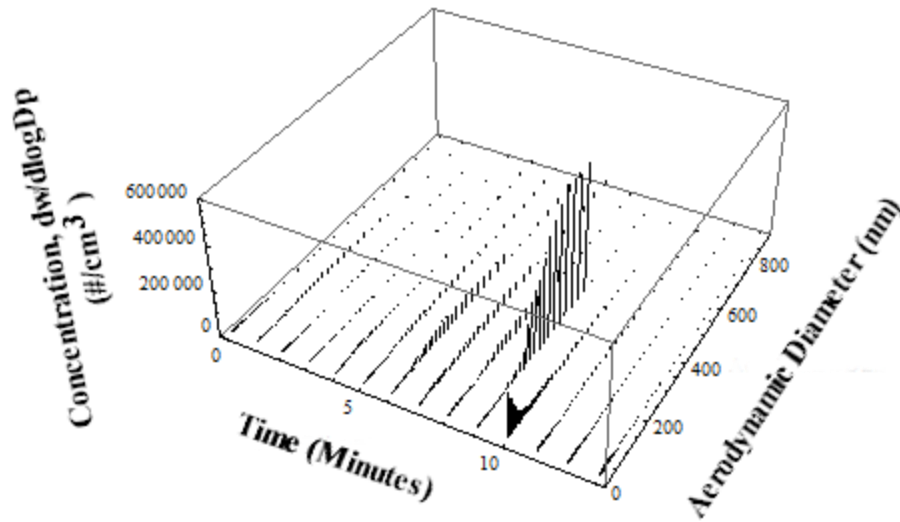
Fig. 5. Particle size distribution for 31 kg and 1500 rpm. The room temperature and average relative humidity were 303 K and 54%, respectively. This graph has been corrected for background.

Additional analysis of the 31 kg data can be seen in Table IV.

TABLE IV

Mean, Standard Deviation, and Median of Particle Size Distribution (diameter in nm) at 31 kg Loading.

31 kg			
Time (min)	Mean	Standard Deviation	Median
0	70	59	50
1	246	130	245
2	211	160	198
3	78	77	46
4	146	74	128
5	282	114	264
6	258	121	245
7	238	135	228
8	266	141	264
9	362	97	378

10	66	83	35
11	167	140	119
12	125	124	62
13	107	111	54

When the load was 56 kg at 1500 rpm, as can be seen in Fig. 6, significant quantities of particles were produced only after about 5 minutes. The size distribution of particles has a peak between 18.1 nm and 25 nm diameters and does not follow a standard Gaussian, lognormal, or exponential distribution pattern due to a peak near the small diameters. Following initial 5 minutes of the experimental run, the particle distribution shifted from a broader shape to a narrower one with concentrations being focused in the smaller ranges. This can be seen in Table V.

TABLE V

Mean, Standard Deviation, and Median of Particle Size Distribution (diameter in nm) at 56 kg Loading.

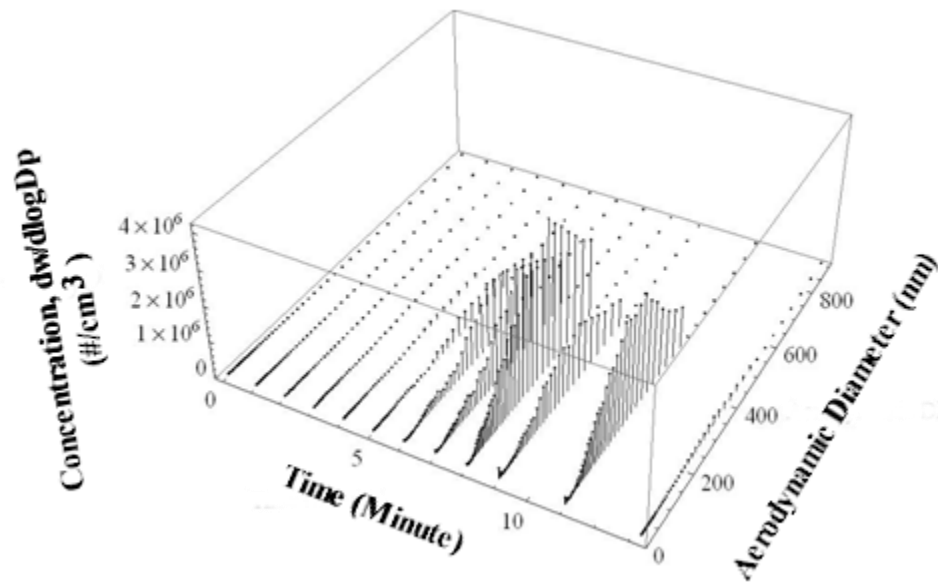| 56 kg			
Time (min)	Mean	Standard Deviation	Median
0	45	23	37
1	49	39	32
2	160	112	119
3	258	162	305
4	365	104	378
5	350	103	352
6	313	118	327
7	294	121	305
8	265	121	264
9	258	122	245
11	250	114	245
13.22	301	107	305

Fig. 6. Particle size distribution for 56 kg and 1500 rpm. The room temperature and average relative

humidity were 303 K and 53%, respectively. This graph has been corrected for background.

For the 56 kg loading test, during the first 5 minutes while no significant numbers of particles were being detected, a visual inspection noted that the contact point was still intact and appeared to be the same as when the test started. As the test progressed, however, the contact point changed from a point to a disk as can be seen in Fig. 7. The fixed sample assumed a concave shape while the rotating sample assumed a convex shape.

Fig. 7. Samples of 56 kg test exhibiting concave/convex shape. Rotated sample on left.

This suggests that at higher load, point contact compressed the samples during the initial period and that this inhibited the initial production of a significant number of particles. After particle formation was observed to start, the formation of the observed concave-convex geometry seems to both suggest and support the existence of this compression phenomenon. Eventually the constant abrasive force started dislodging particles.

In one experiment, the rpm of the shaft to which the sample was attached was changed to 310 rpm and the loading to 22 kg in order to see if the reduced rotation had any immediately observable effect on the particle generation. The results of this run are presented in Fig. 8.
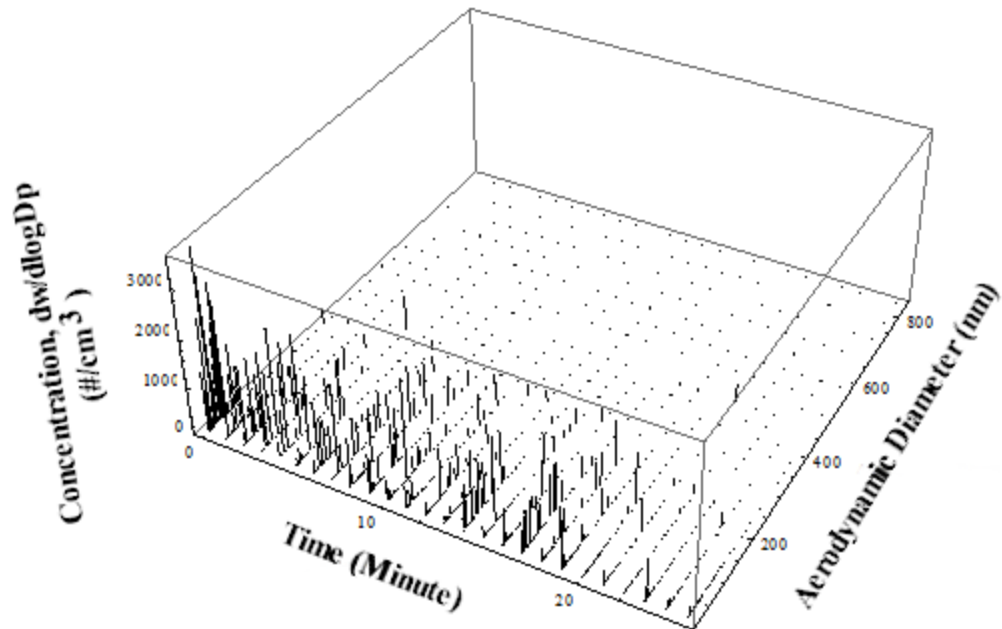
Fig. 8. Particle size distribution for 22 kg and 310 rpm. The room temperature and average relative

humidity were 303 K and 54%, respectively. This graph has been corrected for background.

Again, like in the 10 kg loading test, not many particles were observed. In this instance,

the particles are even smaller than the 10 kg test. Further analysis can be seen in Table

VI.

TABLE VI

Mean, Standard Deviation, and Median of Particle Size Distribution (diameter in nm) at

22 kg Loading.

22 kg			
Time (min)	Mean	Standard Deviation	Median
0	52	51	46
1	58	50	46
2	79	49	62

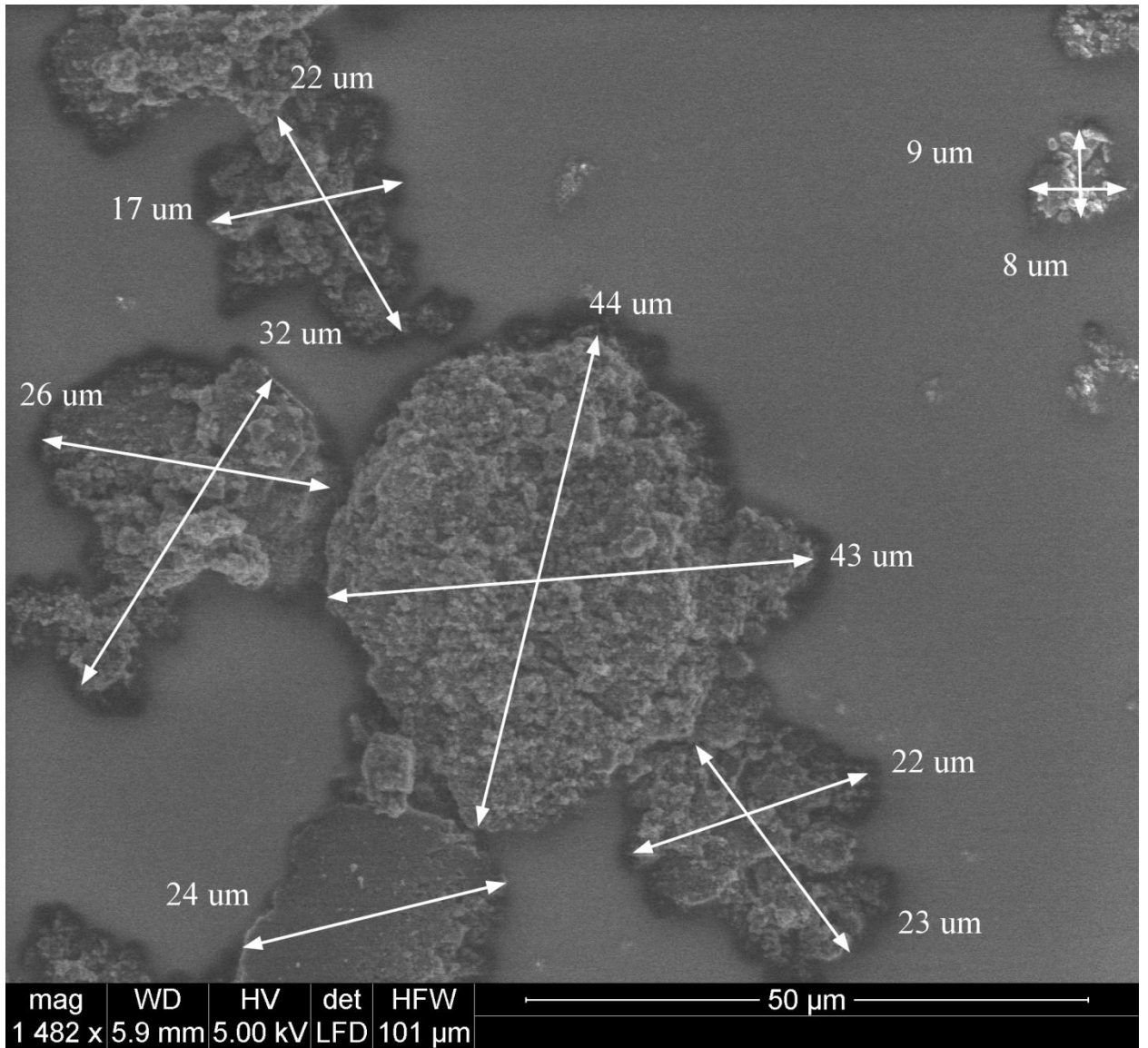|			
3	89	76	62
4	114	108	77
5	93	44	83
6	71	84	50
7	111	77	89
8	126	81	138
9	114	91	89
10	100	74	72
11	132	112	37
12	114	77	89
13	128	108	83
14	74	47	62
15	158	104	198
16	102	98	96
17	90	70	103
18	158	94	184
19	71	72	26
20	184	56	184
21	219	166	138
22	246	97	245
23	44	99	22
24	138	132	198
25	58	141	26

It is possible that the test pebbles might not have been compacted uniformly during their production. There was no mechanism in place to monitor the process quality control during the production of the commercial grade graphite that was used in this study. Abrasion/attrition of an initial outer layer may also partially explain why the particle size distribution was observed to change dramatically.

The data obtained in the present study suggests that the particle generation rate and the particle size distributions obtained from graphite depend on loading, time under load, and the rotational speed at the point of contact. As one might expect, greater loads produced more particles than lesser loads at the same rotational speed. It was also
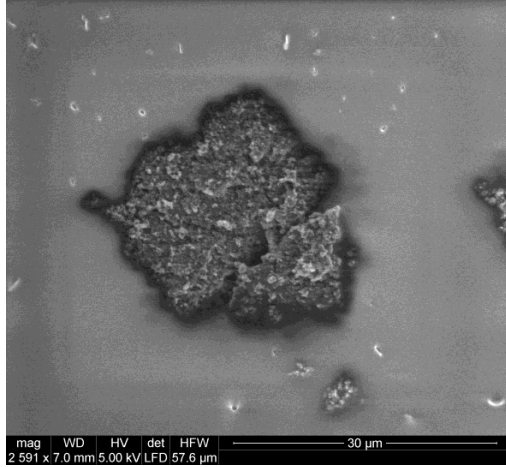
revealed that the particle generation rate is not simply proportional to time but that it can vary quite abruptly with a sudden onset of particle generation occurring only after initial period of apparent inactivity which, again, we hypothesize may be due to an initial compressive stabilization of the graphite surface.
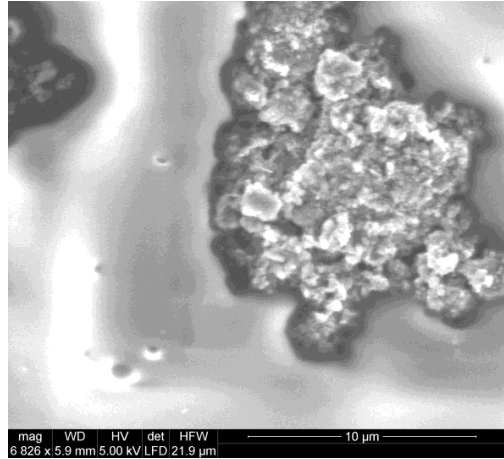
III. B. Shape and Size from SEM Analysis

The graphite particles generated by abrasion were further studied by obtaining their SEM images. These particles were collected from the bottom of the chamber, where they settled, after the abrasion tests were completed. The samples collected from the bottom were sonicated using acetone in an attempt to break them apart. After sonication, several drops of the sonicated solution were placed on the SEM sample holder. The sample was dried at room temperature and then observed in the SEM. As can be seen from Fig. 9, the shape of the particles is non-spherical. They are jagged and the surfaces are porous. As one can see from the scale on the SEM images, there were some particles in the larger size range that could not be detected by the APS™ and SMPS™ due, mainly, to the limitations of these two instruments. As can be seen from these SEM images, some large particles in the micron size range were present. The larger size particles may have resulted from agglomeration of particles falling to the container surface. The SEM images do suggest that the larger particles were a collection of fine particles bound together, however, they were bound strongly enough that they cannot be separated by sonication.
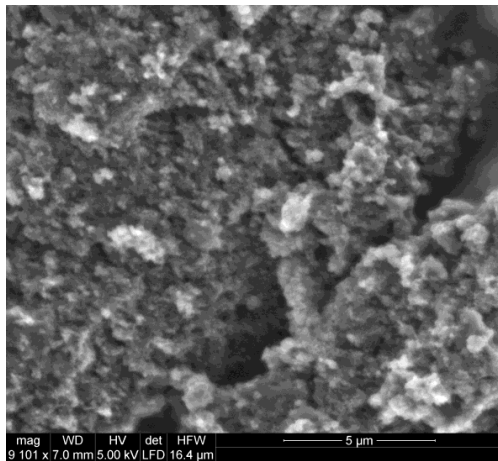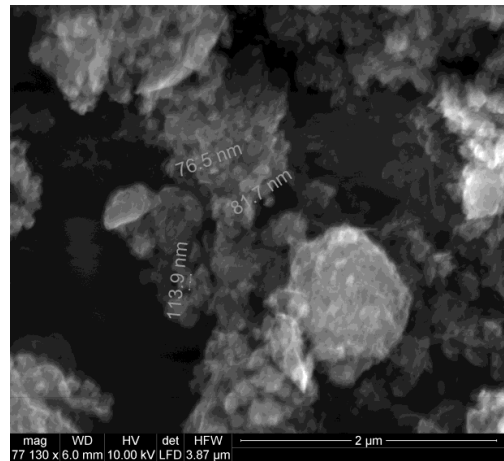
(a) scale 50 μm
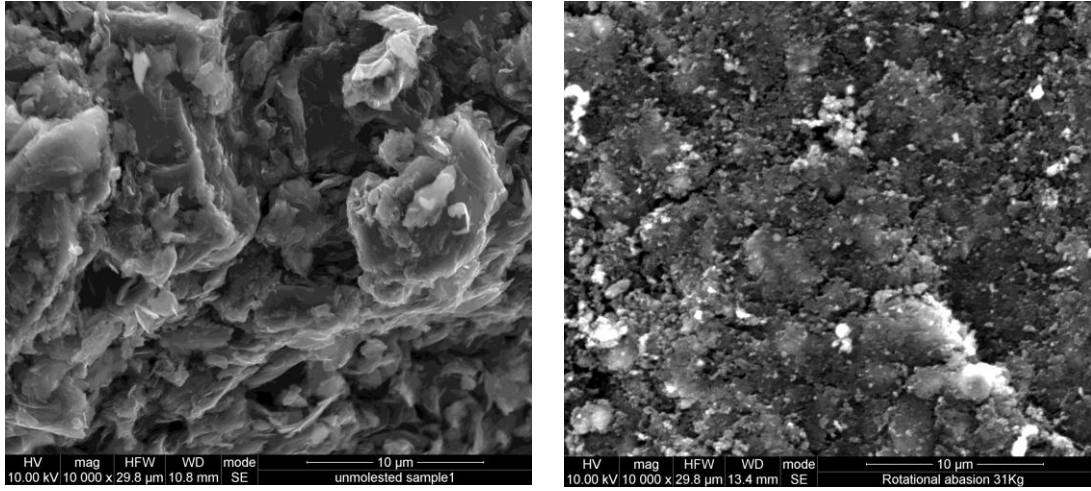
(b) scale 30 μm

(c) scale 10 μm

(d) scale 5 μm

(e) scale 2 μm

Fig. 9. SEM images taken from of particles that settled at the bottom or deposited on the surface of the container

The SEM images of the surface at the point of contact between two hemispheres of the graphite sample, before and after the abrasion test, are compared in Fig. 10. As can be seen from this figure, before the abrasion test, the surface appeared rather rough. As would be expected, this rough surface started to become smoother at the end of the test. Figure 10 also indicates some compaction of the surface.

(a) Before the test   (b) After the test

Fig. 10. SEM images of the surface where two hemispherical graphite samples made contact for the abrasion test.

III.C. BET Surface Area, Pore Volume, and Porosity Analysis

We have carried out measurements of the surface area and pore volume distribution of the unabraded graphite and particles generated. The multipoint Brunauer-Emmett-Teller (BET) method was used to determine the surface area of the particles[23]. We used the nitrogen adsorption isotherm at 77 K which is shown in Fig. 11. BET surface area is obtained using the equation:

$$\frac{1}{W\left(\dfrac{p_0}{p}-1\right)} = \frac{1}{W_m C} + \frac{C-1}{W_m C}\left(\frac{p}{p_0}\right) \tag{3}$$

where W is the weight of the gas adsorbed at a relative pressure, p/p_0, W_m is the weight of adsorbate constituting a mono layer of surface coverage, and C is a constant.

In the BET method, a plot of $\dfrac{1}{W\left(\dfrac{p_0}{p}-1\right)}$ vs. $\dfrac{p}{p_0}$ in the range of $0.05 \leq p/p_0 \leq 0.35$,

which is referred to as the range for monolayer coverage, yields a straight line. The slope

of this line (S) and its intercept (i) are given by:

$$S = \frac{C-1}{W_m C} \tag{4}$$

and:

$$i = \frac{1}{W_m C} \tag{5}$$

Using Eqs. 4 and 5, the monolayer coverage W_m is simply:

$$W_m = \frac{1}{S+i} \tag{6}$$

The total surface area (S_t) can, therefore, be obtained as:

$$S_t = \frac{W_m N A_{CS}}{M} \tag{7}$$

where A_{CS} is the cross-sectional area of the adsorbate molecule which, for nitrogen, is

16.2 Å^2, N is Avogadro's number, M is the molecular weight of the adsorbate, and S_{SP}

the specific surface area of the solid is given by:

$$S_{SP} = \frac{S_t}{W} \tag{8}$$

We have shown adsorption and de-adsorption isotherms for the un-abraded graphite and

the particles in Figs. 11 and 12, respectively. The isotherm data shows little hysteresis.

This is indicative of a straight pore structure and the absence of bottle neck type pores.

The total BET surface area for the un-abraded graphite was found to be 2 m^2 gm^{-1} while

for the particles it was found to be 626 m^2 gm^{-1}. Such a high surface area is indicative of a highly porous material, with significant numbers of pores in the nanometer range. Such a high surface area could provide for substantial fission product adsorption/absorption and reactions.
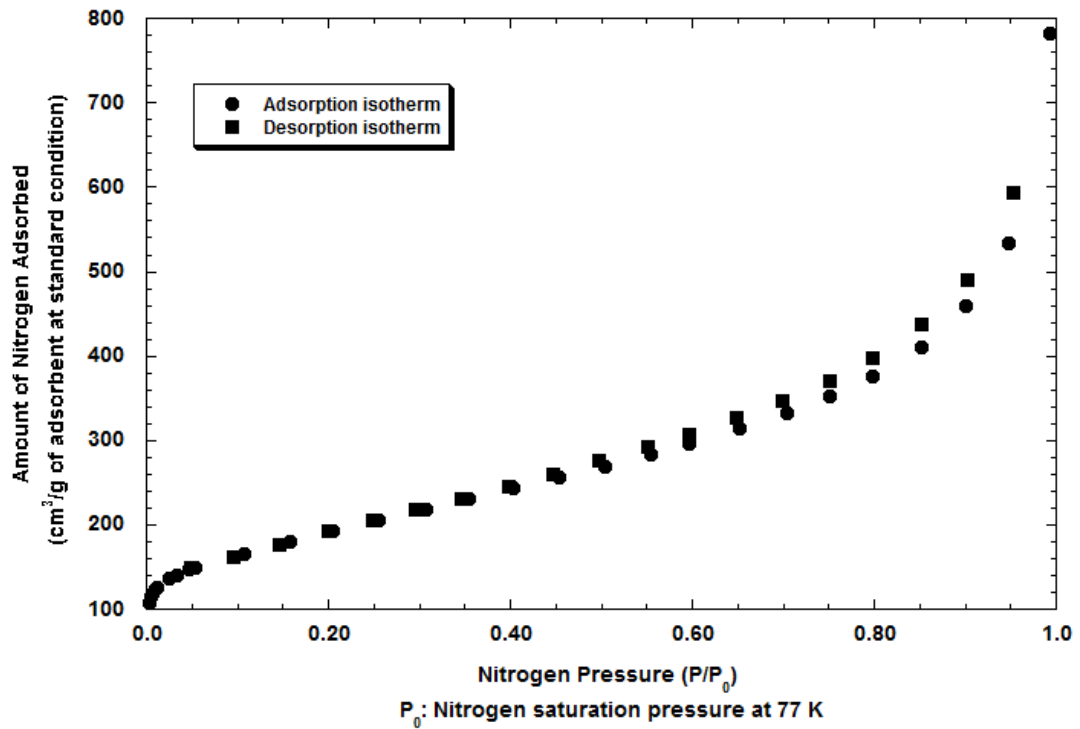

Fig. 11. Isotherm generated from the Quantachrome-Autosorb 1 of particles that settled at the bottom or deposited on the surface of the container.
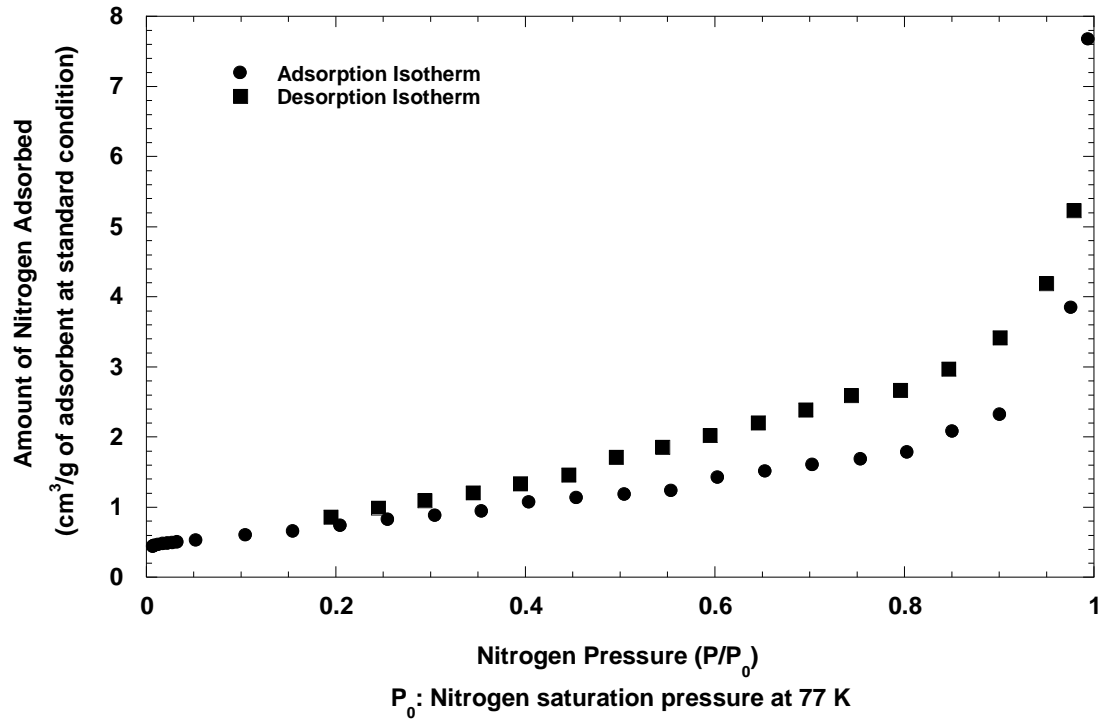
Fig. 12. Nitrogen adsorption-desorption isotherms of unabraded graphite sample at 77 K.

The nitrogen adsorption isotherm data was used to calculate the size distribution of mesopores of the particles the Kelvin equation (Eq. 9)[23]. We assumed, a cylindrical pore geometry and the Kelvin radius of the pore is then given by:

$$r_K = \frac{-2\gamma V_m}{RT \ln\left(\dfrac{p}{p_0}\right)} \qquad (9)$$

where γ is the surface tension of nitrogen at its boiling point, V_m is the molar volume of liquid nitrogen, R is the universal gas constant, T is the boiling point of nitrogen, and

p / p_0 is the relative pressure of nitrogen. The actual pore radius, r_P, is related to the Kelvin radius, r_K, as,

$$r_P = r_K + t \tag{10}$$

Where t is the thickness of the adsorbed layer and is given by:

$$t(\text{Å}) = \frac{4.15}{\log\left(\dfrac{p}{p_0}\right)} \tag{11}$$

We have not explored the microscopic theories of adsorption in the present work to calculate the micropore size distribution. We used the software provided by the Quantachrome Autosorb system to determine the micropore size distribution (this software uses the Generalized Adsorption Isotherm (GAI) equation). The relation between isotherms determined by these microscopic approaches and the experimental isotherm on a porous solid can be interpreted in terms of the Generalized Adsorption Isotherm (GAI) equation:

$$N\left(\frac{p}{p_0}\right) = \int_{W_{\min}}^{W_{\max}} N\left(\frac{p}{p_0}, W\right) f(W) dW \tag{12}$$

where $N(p / p_0)$ is the experimental adsorption isotherm, W is the pore width, $N(p / p_0, W)$ is the isotherm of a single pore of width W, and $f(W)$ is the pore size distribution function. The GAI equation reflects the assumption that the total isotherm consists of a number of individual 'single pore' isotherms multiplied by their relative distribution, $f(W)$, over a range of pore sizes. The set of $N(p / p_0, W)$ isotherms in the kernel of the integral for a given system (adsorbate/adsorbent) can be obtained from either Density Functional Theory or by Monte Carlo computer simulation, and $f(W)$ can

be determined through inversion or minimization. We have used here a Non-Linear Density Functional Theory (NLDFT) isotherm for ($N(p/p_0$, W) appropriate for N_2-carbon system as applicable in the software, but this aspect may need to be studied further.

The pore size distribution is shown in Fig. 13. The data show that the diameter of most of the pores is in the range of 10 to 60 Å. For carbonaceous materials, pores are generally categorized in three size ranges: micropores (diameter, $d < 1$ nm), mesopores (1 nm $< d < 25$ nm), and macropores ($d > 25$ nm). However, it should be noted that this distinction is rather arbitrary. The present sample showed a significant number of pores in the micropore range. Interestingly, the pore size distribution showed two distinct peaks; one at 10 Å (1 nm) and the other one at 50 Å (5 nm). These pores must have been created in the material during abrasion of the pebbles, since unabraded pebbles have very low surface areas and pore volumes.
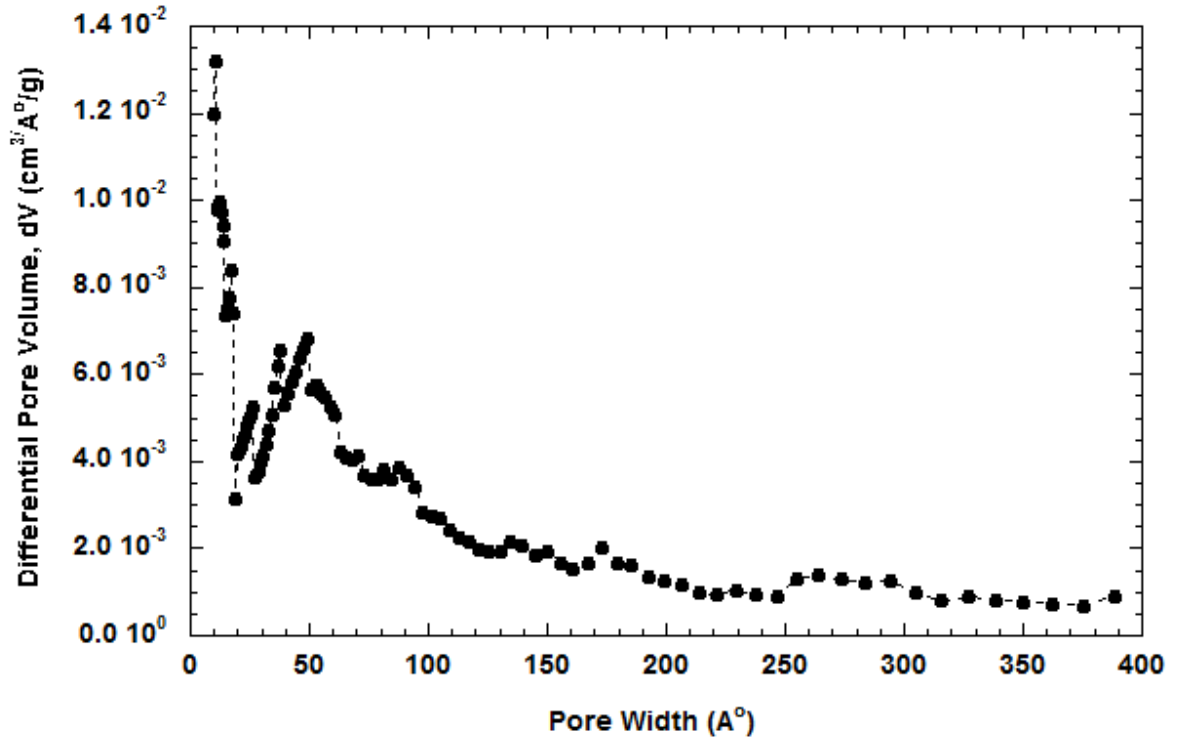
Fig. 13. Pore size distribution particles of that settled at the bottom or deposited on the surface of the container.

The cumulative pore volume calculated from Eqn. 12 confirms the highly porous nature of the particles. This is shown in Fig. 14. The total cumulative pore volume was found to be 1.213 cm^3 gm^{-1}. Since the density of the graphite used to prepare the hemisphere is 1.75 gm cm^{-3}, the porosity of the generated particles is about 68%. Such a porosity again provides access to large surface area for various gaseous fission products to interact with the particles.
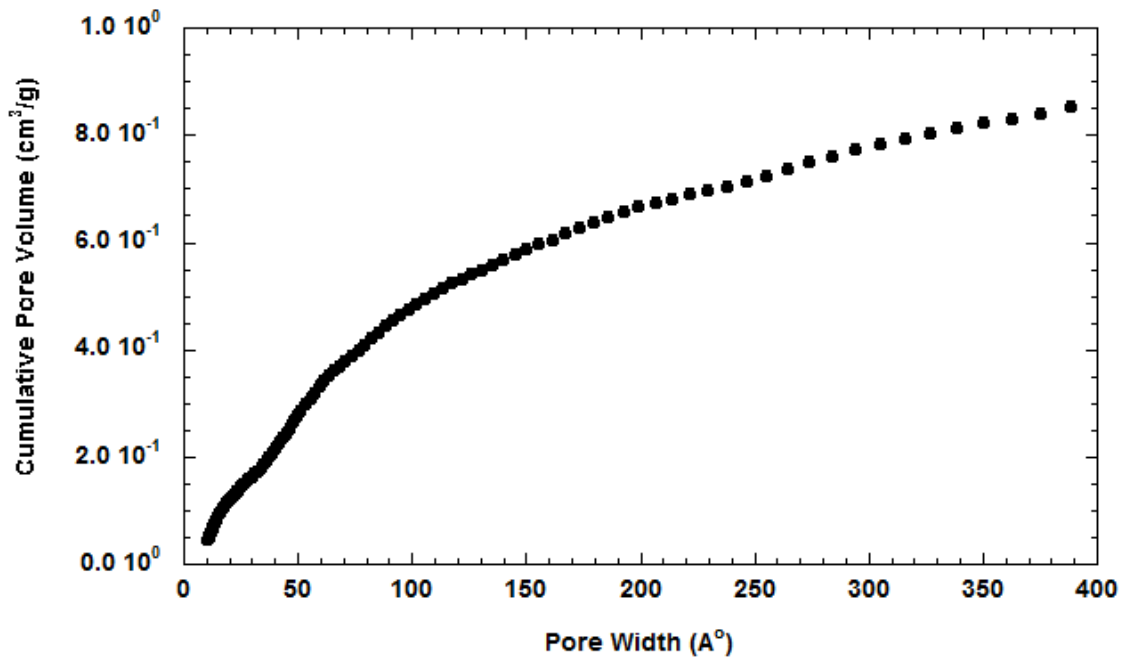

Fig. 14. Cumulative pore volume (cm^3 gm^{-1}) of particles that settled at the bottom or deposited on the surface of the container.

IV. CONCLUSIONS.

An experimental system was designed and constructed to generate graphite particles (dust) through abrasion of graphite pebbles. The size distributions and the concentrations of the graphite particles generated by abrasion are found to be dependent on time and loading. The time of pebble abrasion has a strong effect on the particle generation rate as well as on the size distribution. A significant number of particles were generated in the nanosize range. Both the SEM micrographs and surface area analysis showed that the particles are very porous and contained significant numbers of micropores.

Our principle goal was to devise a system for the abrasive generation of graphite dust particles that might be realized during normal operations of a PBR and to demonstrate its functionality. To this latter end, the current work used a commercial grade of graphite. This was, however, sufficient to demonstrate the usefulness of the system and to provide many insights. With minor modifications, sliding abrasion between graphite spheres and sliding and rotational abrasion of graphite spheres with flat and curved surfaces of containment vessel alloy and other structural material may also be studied. The capability also exists with this system to control the gas mixture present during abrasion (including the humidity). As currently configured, the test system is intended only for abrasion studies at or near room temperature. With some more extensive modification, however, a very similar system might be constructed that would be capable of handling experiments at elevated temperatures. At this point, our future plans are to extend the current measurements to various reactor grades of graphite and to explore the role of the gas mixture (He predominately) in abrasive dust generation.

REFERENCES

1.   L. TAN, T. R. ALLEN, J. D. HUNN AND J. H. MILLER, "EBSD for microstructure and property characterization of the SiC-coating in TRISO fuel particles," *Journal of Nuclear Materials* **372** (2-3), 400-404 (2008).

2.   K. VERFONDERN, et al., "Fuel Performance and Fission Product Behavior in Gas Cooled Reactors," *IAEA-ThCDOC-978*. (1997).

3.   F. W. BACH, P. WILK AND M. LINDE, "Fractionalization of Graphitic Reactor Components," Conference Proceedings: Kontec 2001, 606-616 (2001).

4.   S. J. BALL, T. D. BURCHELL, W. R. CORWIN, S. E. FISHER, C. W. FORSBERG, R. N. MORRIS AND D. L. MOSES, Report No. ORNL/TM-2007/228, 2008.

5.   B. BISPLINGHOF, H. BRUCHER, J. FACHINGER AND M. LOCHNY, "Radiochemical Characterisation of Graphite from Julich Experimental Reactor (AVR)," *Nuclear Energy* **39** (5), 311 (2000).

6.   S. SAISHU AND T. INOUE, "Technical Development of Graphite Waste Treatment in NUPEC," IAEA Technical Committee Meeting on Nuclear Graphite Waste Management (1999).

7.   X. LUO, S. YU, X. SHENG AND S. HE, "Temperature effect on IG-11 graphite wear performance," *Nuclear Engineering and Design* **235** (21), 2261-2274 (2005).

8.   X. SHENG, S. YU, X. LUO AND S. HE, "Wear behavior of graphite studies in an air-conditioned environment," *Nuclear Engineering & Design* **223** (2), 109 (2003).

9.   L. XIAOWEI, Y. SUYUAN, S. XUANYU AND H. SHUYAN, "The influence of roughness on tribological properties of nuclear grade graphite," *Journal of Nuclear Materials* **350** (1), 74-82 (2006).

10.   Z. XUEYING, H. MATT, W. SAWYER AND P. SCOTT, "Thermally Activated Friction," *Tribology Letters* **27** (1), 113-117 (2007).

11.   X. LUO, X. LI AND S. YU, "Nuclear graphite friction properties and the influence of friction properties on the pebble bed," *Nuclear Engineering & Design* **240** (10), 2674-2681 (2010).

12.   X. W. LUO, S. Y. YU AND X. Y. SHENG, "Graphite friction coefficient for various conditions," *Science in China, Series A - Mathematics Physics Astronomy* **44**, 248-252 (2001).

13.	I. C. ROSELMAN AND D. TABOR, "The friction and wear of individual carbon fibres," *Journal of Physics D: Applied Physics* **10** (8), 1181-1194 (1977).

14.	P. V. K. PORGESS AND H. WILMAN, "Surface Re-orientation, Friction and Wear, in the Unidirectional Abrasion of Graphite," *Proceedings of the Physical Society* **76** (4), 513-525 (1960).

15.	S. F. FOERSTER, M. Y. LOUGE, H. CHANG AND K. ALLIA, "Measurements of the collision properties of small spheres," *Phys Fluids* **6**, 1108-1115 (1995).

16.	C. HOLMES, B. W. DRINKWATER AND J. F. B. PAYNE, "The influence of interface effects on the rocking behaviour of graphite blocks," *Journal of Strain Analysis for Engineering Design* **39** (4), 359-370 (2004).

17.	W. C. HINDS, *Aerosol Technology: Properties, Behavior, and Measurement of Airborne Particles*, 2nd Ed., New York: J. Wiley, 1999.

18.	Data Merge Software Module Manual, Model 390069, TSI Inc., MN USA, 2010

19.	R. L. BUCKLEY, & S. K. LOYALKA, "Cunningham correction factor and accommodation coefficient: Interpretation of millikan's data," *Journal of Aerosol Science*, 20(3), 347-349 (1989).

20.	D. V. COLAMECO, K. N. IVANOV, R. H. PRINSLOO, D. I. TOMASEVIC AND S. THERON, "A Comparison Between Recent Advances in Cylindrical Nodal Diffusion Methods," *Journal of Engineering for Gas Turbines and Power* **132** (3) (2010).

21.	Z. ZHANG, Z. WU, D. WANG, Y. XU, Y. SUN, F. LI AND Y. DONG, " Current status and technical description of Chinese 2×250MWth HTR-PM demonstration plant," *Nuclear Engineering and Design* **239** (7), 1212-1219 (2009).

22.	A. M.-E.-A. OUGOUAG AND W. K. TERRY, "A Preliminary Study of the Effect of Shifts in Packing Fraction on k-effective in Pebble-Bed Reactors," M&C 2001 Salt Lake City, Utah, USA, September (2001).

23.	AUTOSORB-I, operating manual v1.51, Quantachrome Instruments, FL USA, 2010